exoALMA. VII. Benchmarking hydrodynamics and radiative transfer codes

Bae, J.; Flock, M.; Izquierdo, A.; Kanagawa, K.; Ono, T.; Pinte, C.; ... ; Yoshida, T.C.

The Astrophysical Journal Letters, 984:L12 (14pp), 2025 May 1 https://doi.org/10.3847/2041-8213/adc436

exoALMA. VII. Benchmarking Hydrodynamics and Radiative Transfer Codes

Jaehan Bae[1], Mario Flock[2], Andrés Izquierdo[1,3,4,24], Kazuhiro Kanagawa[5], Tomohiro Ono[6], Christophe Pinte[7,8], Daniel J. Price[8], Giovanni P. Rosotti[9], Gaylor Wafflard-Fernandez[7], Geoffroy Lesur[7], Frédéric Masset[10], Sean M. Andrews[11], Marcelo Barraza-Alfaro[12], Myriam Benisty[2,13], Gianni Cataldi[14], Nicolás Cuello[7], Pietro Curone[15,16], Ian Czekala[17], Stefano Facchini[15], Daniele Fasano[13], Maria Galloway-Sprietsma[1], Cassandra Hall[18,19,20], Iain Hammond[8], Jane Huang[21], Giuseppe Lodato[15], Cristiano Longarini[15,22], Jochen Stadler[13], Richard Teague[12], David J. Wilner[11], Andrew J. Winter[2,13], Lisa Wölfer[12], and Tomohiro C. Yoshida[14,23]

[1] Department of Astronomy, University of Florida, Gainesville, FL 32611, USA
[2] Max-Planck Institute for Astronomy (MPIA), Königstuhl 17, 69117 Heidelberg, Germany
[3] Leiden Observatory, Leiden University, P.O. Box 9513, NL-2300 RA Leiden, The Netherlands
[4] European Southern Observatory, Karl-Schwarzschild-Str. 2, D-85748 Garching bei München, Germany
[5] College of Science, Ibaraki University, 2-1-1 Bunkyo, Mito, Ibaraki 310-8512, Japan
[6] School of Natural Sciences, Institute for Advanced Study, Princeton, NJ 08544, USA
[7] University Grenoble Alpes, CNRS, IPAG, 38000 Grenoble, France
[8] School of Physics and Astronomy, Monash University, VIC 3800, Australia
[9] Dipartimento di Fisica, Università degli Studi di Milano, Via Celoria 16, I-20133 Milano, Italy
[10] Instituto de Ciencias Físicas, Universidad Nacional Autonoma de México, Av. Universidad s/n, 62210 Cuernavaca, Mor., México
[11] Center for Astrophysics—Harvard & Smithsonian, Cambridge, MA 02138, USA
[12] Department of Earth, Atmospheric, and Planetary Sciences, Massachusetts Institute of Technology, Cambridge, MA 02139, USA
[13] Université Côte d'Azur, Observatoire de la Côte d'Azur, CNRS, Laboratoire Lagrange, 06300 Nice, France
[14] National Astronomical Observatory of Japan, 2-21-1 Osawa, Mitaka, Tokyo 181-8588, Japan
[15] Dipartimento di Fisica, Università degli Studi di Milano, Via Celoria 16, 20133 Milano, Italy
[16] Departamento de Astronomía, Universidad de Chile, Camino El Observatorio 1515, Las Condes, Santiago, Chile
[17] School of Physics & Astronomy, University of St. Andrews, North Haugh, St. Andrews KY16 9SS, UK
[18] Department of Physics and Astronomy, The University of Georgia, Athens, GA 30602, USA
[19] Center for Simulational Physics, The University of Georgia, Athens, GA 30602, USA
[20] Institute for Artificial Intelligence, The University of Georgia, Athens, GA, 30602, USA
[21] Department of Astronomy, Columbia University, 538 W. 120th Street, Pupin Hall, New York, NY 10027, USA
[22] Institute of Astronomy, University of Cambridge, Madingley Road, CB3 0HA, Cambridge, UK
[23] Department of Astronomical Science, The Graduate University for Advanced Studies, SOKENDAI, 2-21-1 Osawa, Mitaka, Tokyo 181-8588, Japan
Received 2024 December 2; revised 2025 February 10; accepted 2025 March 4; published 2025 April 28

Abstract

Forward modeling is often used to interpret substructures observed in protoplanetary disks. To ensure the robustness and consistency of the current forward-modeling approach from the community, we conducted a systematic comparison of various hydrodynamics and radiative transfer codes. Using four grid-based hydrodynamics codes (`FARGO3D`, `Idefix`, `Athena++`, and `PLUTO`) and a smoothed-particle hydrodynamics code (`Phantom`), we simulated a protoplanetary disk with an embedded giant planet. We then used two radiative transfer codes (`mcfost` and `RADMC-3D`) to calculate disk temperatures and create synthetic ^{12}CO cubes. Finally, we retrieved the location of the planet from the synthetic cubes using `DISCMINER`. We found strong consistency between the hydrodynamics codes, particularly in the density and velocity perturbations associated with planet-driven spirals. We also found a good agreement between the two radiative transfer codes: the disk temperature in `mcfost` and `RADMC-3D` models agrees within $\lesssim$3% everywhere in the domain. In synthetic ^{12}CO channel maps, this results in brightness temperature differences within $\pm$1.5 K in all our models. This good agreement ensures consistent retrieval of planet's radial/azimuthal location with only a few percent of scatter, with velocity perturbations varying $\lesssim$20% among the models. Notably, while the planet-opened gap is shallower in the `Phantom` simulation, we found that this does not impact the planet location retrieval. In summary, our results demonstrate that any combination of the tested hydrodynamics and radiative transfer codes can be used to reliably model and interpret planet-driven kinematic perturbations.

Unified Astronomy Thesaurus concepts: Protoplanetary disks (1300); Planetary-disk interactions (2204); Hydrodynamical simulations (767); Radiative transfer simulations (1967)

1. Introduction

Recent high-resolution observations have revealed a range of substructures in protoplanetary disks, including gaps, rings, crescents, and spirals in the dust continuum and velocity kinks in molecular line channel maps. While unequivocally connecting these substructures to their cause(s) is not straightforward (see, e.g., reviews by S. M. Andrews 2020 and J. Bae et al.

[24] NASA Hubble Fellowship Program Sagan Fellow.

2023), one exciting possibility is that embedded protoplanets have created the observed substructures.

As protoplanets grow, they perturb their natal protoplanetary disks, producing observable signatures. While these perturbations manifest in various forms, in this Letter we focus on kinematic perturbations observable with radio interferometric molecular line observations. In the vicinity of a protoplanet, spiral arms launched by the protoplanet induce strong perturbations in the density, temperature, and velocity of the background disk. These perturbations can manifest as velocity kinks in channel maps and/or Doppler flips in velocity centroid maps (see review by C. Pinte et al. 2023 and references therein). Because these perturbations are generally strongest near protoplanets, velocity kinks and Doppler flips offer an opportunity to locate the protoplanet. In a more global scale, spirals launched by a protoplanet exchange angular momentum with the disk gas, causing an annular gap to open around the protoplanet's orbit (D. N. C. Lin & J. C. B. Papaloizou 1993). The radially varying pressure gradient associated with the gap modulates the azimuthal velocity of the disk gas. As a result, inward to the protoplanet's orbit, the gas rotates at a sub-Keplerian speed, while outward to the orbit, the gas rotates at a super-Keplerian speed (K. D. Kanagawa et al. 2015). Because the width and depth of a planet-opened gap depend on the mass of the embedded protoplanet, the observed azimuthal velocity of the disk gas can be used to infer the protoplanet's mass (S. Zhang et al. 2018; H.-G. Yun et al. 2019).

Hydrodynamic planet–disk interaction simulations, combined with radiative transfer calculations, can give us a deeper understanding of the nature of observed substructures. For example, this forward-modeling approach enables one to infer the location and mass of the planet responsible for observed substructures (e.g., C. Pinte et al. 2018; J. Bae et al. 2019, 2021), which can offer crucial insights into planet-formation processes. However, while there had been previous efforts to compare properties of the gap a planet opens and the gravitational torque a planet exerts on its protoplanetary disks using various hydrodynamics codes (M. de Val-Borro et al. 2006), to date, no systematic hydrodynamics or radiative transfer benchmark tests comparing kinematic perturbations induced by planets embedded in their birth protoplanetary disks have been carried out. To this end, in this Letter we tested if various hydrodynamics and radiative transfer codes produce consistent results. We benchmarked five hydrodynamics codes, namely `FARGO3D` (P. Benítez-Llambay & F. S. Masset 2016), `Idefix` (G. R. J. Lesur et al. 2023), `Athena++` (J. M. Stone et al. 2020), `PLUTO` (A. Mignone et al. 2007), and `Phantom` (D. J. Price et al. 2018) and two radiative transfer codes, `mcfost` (C. Pinte et al. 2006; C. Pinte et al. 2009) and `RADMC-3D` (C. P. Dullemond et al. 2012), which are some of the most widely used codes from the community. Our benchmark test considered a protoplanetary disk with an embedded giant planet having a mass that is 10^{-3} of the central star, which corresponds to about a Jupiter mass in a system with a solar-mass central star.

This Letter is organized as follows. In Section 2, we describe the planet–disk interaction simulation setup and compare the hydrodynamics simulation results. In Section 3, we describe the radiative transfer simulation setup and compare disk temperatures and synthetic ^{12}CO cubes. We retrieve the planet location in the synthetic cubes using `DISCMINER` and present the results in Section 4. We summarize our findings and conclude in Section 5.

2. Hydrodynamic Simulations

2.1. Grid-based Hydrodynamics Simulation Setup

Grid-based simulations were carried out using four hydrodynamics codes: FARGO3D[25] version 2.01 (P. Benítez-Llambay & F. S. Masset 2016), `Idefix`[26] version 1.1.0 (G. R. J. Lesur et al. 2023), `Athena++`[27] version 21.0 (J. M. Stone et al. 2020), and `PLUTO`[28] version 4.3 (A. Mignone et al. 2007). While we refer the reader to the relevant papers cited in the preceding sentence for technical details of these codes, we emphasize their fundamental differences in solving hydrodynamic equations. Among the grid-based codes, `FARGO3D` employs a finite-difference scheme, which directly approximates derivatives in the differential form of conservation equations. The other three codes, namely `Idefix`, `Athena++`, and `PLUTO`, utilize a finite-volume scheme, which works with the integral form of conservation equations and computes intercell fluxes through Riemann solvers. These methodological differences can influence how each code handles discontinuities between grid cells and conserves physical quantities. It is thus crucial to verify that results obtained with these codes agree with each other.

For all the grid-based simulations presented in this Letter, we used the orbital advection algorithm Fast Advection in Rotating Gaseous Objects (FARGO; F. Masset 2000), which enables us to have a much larger time step by subtracting the azimuthally averaged velocity, although we ran additional simulations without implementing FARGO and confirmed that the outcome of the simulations does not depend on the use of the FARGO algorithm.

2.1.1. Simulation Domain and Numerical Resolution

We used three-dimensional spherical coordinates (r, θ, ϕ). Throughout this Letter, we use r, θ, and ϕ to denote the spherical radius, meridional angle, and azimuthal angle in spherical coordinates, while we use $R \equiv r\sin\theta$ and $Z \equiv r\cos\theta$ to denote the cylindrical radius and height in cylindrical coordinates. The simulation domain extends from $r_{\rm in} = 0.3$ to $r_{\rm out} = 3.0$ in r in the code unit, from $\theta_{\rm min} = \pi/2 - \arctan(0.5)$ to $\theta_{\rm max} = \pi/2 + \arctan(0.5)$ in θ, and from $\phi_{\rm min} = -\pi$ to $\phi_{\rm max} = \pi$ in ϕ. We used 288 logarithmically spaced grid cells in r, 128 linear grid cells in θ, and 784 linear grid cells in ϕ, respectively. With this setup, we achieved $\Delta r \simeq r\Delta\theta \simeq r\Delta\phi \simeq 0.008$ at the radial location of the planet ($r = 1$), a numerical resolution allowing about 12 grid cells per scale height, which was shown to be sufficient for numerical convergence (K. Chen & R. Dong 2024).

2.1.2. Initial Disk Setup

The disk temperature has a power-law profile as a function of the cylindrical radius R, with a slope $q = -0.5$:

$$T(R) = T_p(R/R_p)^q. \quad (1)$$

[25] https://github.com/FARGO3D/fargo3d
[26] https://github.com/idefix-code/idefix/releases/tag/v1.1
[27] https://github.com/PrincetonUniversity/athena/releases/tag/v21.0-dev
[28] https://plutocode.ph.unito.it

Here, R_p is the radial distance between the star and the planet, and T_p is the temperature at $R = R_p$. We chose T_p such that the disk aspect ratio H/R at $R = R_p$ is 0.1, where H denotes the disk scale height. This disk aspect ratio is close to the aspect ratio at the radial location of the planetary candidates identified in C. Pinte et al. (2025) when we adopt the temperature profile inferred in M. Galloway-Sprietsma et al. (2025). We assumed that the disk is vertically isothermal and adopted an isothermal equation of state. Under this assumption, the gas pressure P, gas density ρ, and sound speed c_s satisfy $P = \rho c_s^2$.

In reality, the temperature structure of protoplanetary disks is more complex than the simplified temperature structure we adopted. The disk temperature is vertically stratified as the stellar irradiation diminishes toward the disk midplane (E. I. Chiang & P. Goldreich 1997; P. D'Alessio et al. 1998). In addition, spirals driven by a forming planet can produce shock/compressional heating (A. J. W. Richert et al. 2015; W. Lyra et al. 2016) and/or can cast shadows, modifying the stellar radiation field (D. Muley et al. 2024), all of which can alter the underlying temperature structure. However, we expect the difference in the velocity perturbations at the vicinity of the planet in isothermal simulations and those in more realistic simulations to be rather minor as shown in C. Pinte et al. (2019) where planet-driven velocity perturbations are compared between an isothermal simulation and one where the disk temperature is regularly updated by running radiative transfer calculations.

We initialized the gas density to satisfy the vertical force balance:

$$\rho(R, Z) = \rho_p \left(\frac{R}{R_p}\right)^p \exp\left(\frac{GM_*}{c_s^2}\left[\frac{1}{\sqrt{R^2 + Z^2}} - \frac{1}{R}\right]\right). \quad (2)$$

Here, G is the gravitational constant, and M_* is the stellar mass. We chose ρ_p such that the total initial disk mass is $0.01\,M_\odot$. Note, however, that the hydrodynamic simulations we carried out are scalable, and the outcome does not depend on the choice of the disk mass; the disk mass only becomes relevant in radiative transfer calculations. We adopted $p = -2.25$ such that the surface density follows $\Sigma \propto R^{-1}$.

The angular velocity Ω was initialized to satisfy the radial force balance:

$$\Omega(R, Z) = \Omega_K \left[\left(p + q\right)\left(\frac{H}{R}\right)^2 + (1 + q) - \frac{qR}{\sqrt{R^2 + Z^2}}\right]^{1/2} \quad (3)$$

where $\Omega_K = \sqrt{GM_*/R^3}$ is the Keplerian angular velocity. The initial azimuthal velocity was set to $v_\phi = R\Omega$. The initial radial and meridional velocities were set to zero ($v_r = v_\theta = 0$).

We adopted kinematic viscosity characterized by $\nu = 10^{-5}$. In terms of the Shakura–Sunyaev viscosity parameter α (N. I. Shakura & R. A. Sunyaev 1973), this kinematic viscosity is equivalent to $\alpha = 10^{-3}$ at the radial location of the planet.

2.1.3. Planet Potential

We considered a planet having a mass $M_p = 10^{-3} M_*$. For a solar-mass star, this planet mass corresponds to about a Jupiter mass, which is close to the lower limit we expect to detect in exoALMA-quality data (C. Pinte et al. 2025). The planet potential Φ_p is smoothed following

$$\Phi_p = -\frac{GM_p}{d}\left[\left(\frac{d}{\epsilon}\right)^4 - 2\left(\frac{d}{\epsilon}\right)^3 + 2\left(\frac{d}{\epsilon}\right)\right] \quad (4)$$

when $d \leqslant \epsilon$, where d is the distance between the planet and the grid cell in question and $\epsilon = 3\Delta r \simeq 0.024$, where $\Delta r \simeq 0.008$ is the size of the grid cell at the location of the planet. When $d > \epsilon$, $\Phi_p = -GM_p/d$.

The mass of the planet was ramped up following

$$M_p(t) = M_{p,\mathrm{final}} \sin^2\left(\frac{t}{\tau_{\mathrm{ramp}}}\frac{\pi}{2}\right), \quad (5)$$

where $M_{p,\mathrm{final}} = 10^{-3} M_*$ and $\tau_{\mathrm{ramp}} = 100$ orbits at the radial location of the planet. No gas accretion onto the planet is allowed, so the planet mass is fixed to $10^{-3} M_*$ after 100 orbits. We fixed the planet on a circular orbit and did not allow orbital migration.

2.1.4. Boundary Conditions

At the inner and outer radial boundaries, we adopted the symmetric boundary condition although the choice of radial boundary condition should not have a significant impact on the outcome because we implemented a wave-killing zone at the radial boundaries (M. de Val-Borro et al. 2006). The damping function was written as

$$\frac{dX(r)}{dt} = -\left(\frac{X(r) - X_0(r)}{\tau_{\mathrm{damp}}}\right) f(r), \quad (6)$$

where X is density or velocity and X_0 is the initial value of the variable X. The inner damping zone was located between $r_1 = r_{\mathrm{in}} = 0.3$ and $r_2 = 0.357$, where we set the function $f(r)$ at the inner radial boundary $f_{\mathrm{in}}(r)$ to

$$f_{\mathrm{in}}(r) = 1 - \sin^2\left[\frac{\pi}{2}\frac{(r - r_1)}{(r_2 - r_1)}\right]. \quad (7)$$

The outer damping zone was located between $r_1 = 2.52$ and $r_2 = r_{\mathrm{out}} = 3.0$. The function $f(r)$ at the outer radial boundary, $f_{\mathrm{out}}(r)$, is given by

$$f_{\mathrm{out}}(r) = \sin^2\left[\frac{\pi}{2}\frac{(r - r_1)}{(r_2 - r_1)}\right]. \quad (8)$$

The damping timescale τ_{damp} at the inner/outer radial boundary was given by 1% of the orbital timescale at the inner/outer edge of the domain.

At the meridional boundaries $\theta = \theta_{\mathrm{min}}$ and $\theta = \theta_{\mathrm{max}}$, we adopted the symmetric boundary condition for v_r and v_ϕ. We adopted the antisymmetric boundary condition for v_θ such that $v_\theta = 0$ at the meridional boundary and that the meridional velocity in the active zone and the meridional velocity in the ghost zone, referring to a few extra cells beyond the boundary of the simulation domain, satisfy v_θ (ghost) $= -v_\theta$ (active). The density in the ghost zone was set to satisfy the vertical hydrostatic equilibrium (J. Bae et al. 2016):

$$\frac{1}{\rho}\frac{\partial}{\partial\theta}(\rho c_s^2) = \frac{v_\phi^2}{\tan\theta}. \quad (9)$$

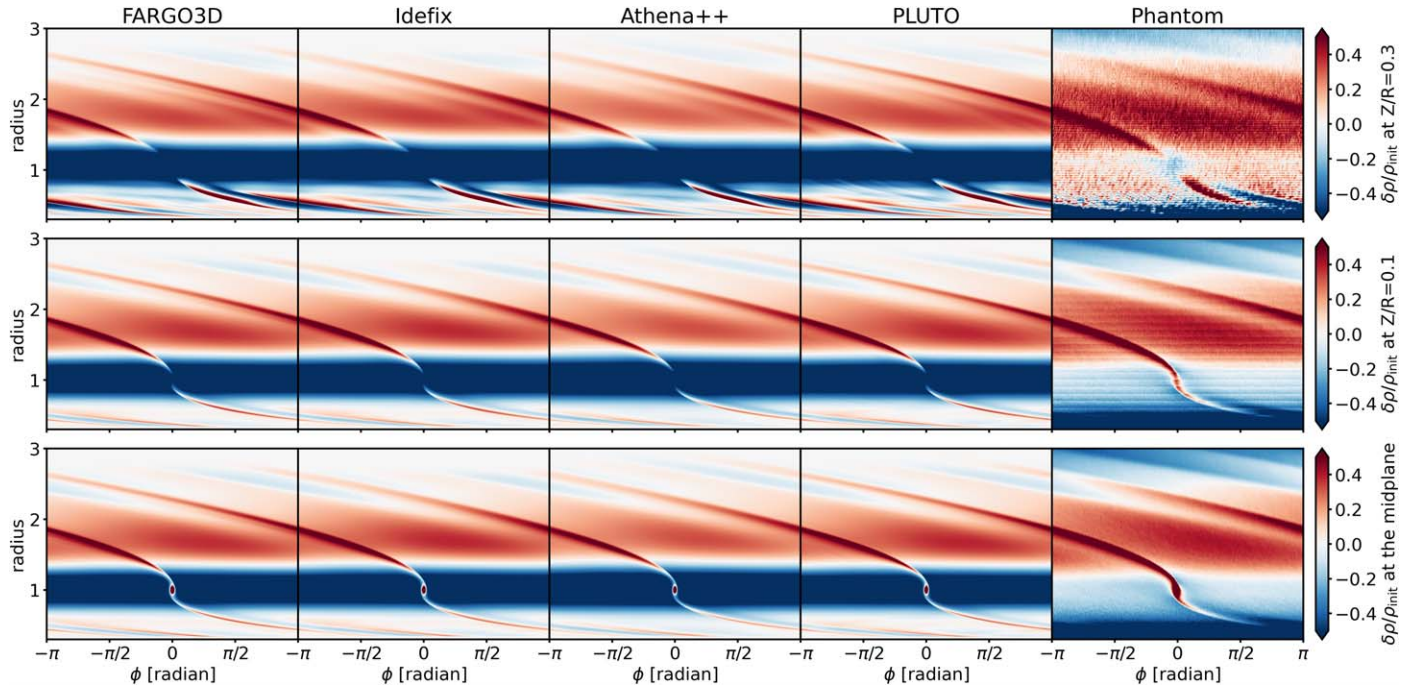

Figure 1. Perturbed density (normalized by the initial density) $\delta\rho/\rho_{\rm init}$ at (top panels) $Z/R = 0.3$ (three scale heights above the midplane at $R = 1$), (middle panels) $Z/R = 0.1$ (one scale height above the midplane at $R = 1$), and (bottom panels) midplane. From left to right, results with `FARGO3D`, `Idefix`, `Athena++`, `PLUTO`, and `Phantom`. At high altitudes, `Phantom` results appear noisy because of the small number of SPH particles in the low-density regions.

2.2. Smoothed-particle Hydrodynamics Simulation Setup

The smoothed-particle hydrodynamics (SPH) simulation was carried out using the code `Phantom`[29] version 2022.0.1 (D. J. Price et al. 2018). `Phantom` solves the equations of hydrodynamics in Lagrangian form. The fluid is discretized onto a set of particles of mass and thus `Phantom` is mesh free by construction. We refer the reader to D. J. Price et al. (2018) for further details on the code.

We initialized the disk based on the grid-based simulation setup described in Section 2.1.2. However, due to the intrinsic differences between grid-based and SPH codes, the exact setup differs inevitably, and we focus on describing these differences below. We used 10 million SPH particles, initially placed between $r = 0.3$ and $r = 3$. Compared to grid-based simulations, SPH simulations do not define a mesh, so particles can freely pass the initial inner/outer radii. We employed a fixed inner boundary at $r = 0.2$ inside of which particles are removed from the simulation. This, and the spreading of the outer disk, mean that the mass (and resolution) enclosed between $r = 0.3$ and $r = 3$ depletes with time, in contrast to the damping boundary conditions employed in the grid-based codes where arbitrary amounts of mass are continuously injected or removed in the damping zones to maintain the initial density profile in the damping zone. We found that about 30% of the initial disk mass is lost through the inner boundary after 500 orbits. Unlike some previous `Phantom` simulations where the mass lost from the disk is added to the star, we fixed the stellar mass to be consistent with grid-based simulations. Another difference compared with grid-based simulations is that the numerical resolution of SPH simulations depends on the local density and thus varies across the simulation domain and over time. This density dependency allows the best numerical resolution in the regions of high density, such as the disk midplane, while the decrease in the density, which can happen near the surface or within a planet-carved gap, results in poor numerical resolution.

We embedded a planet in the disk orbiting at $r = 1$, having a mass $M_p = 10^{-3}M_*$. The potential of the planet was ramped up over the initial 100 orbits, consistently with grid-based simulations. The planet was implemented as a prescribed potential consistently with grid-based simulations; however, note that this is different from the usual approach in `Phantom` simulations where sink particles are used to model planets in a way that explicitly conserves momentum (M. R. Bate et al. 1995). Using a prescribed potential fixes the planet on a circular orbit and does not allow for orbital migration.

We added a fixed kinematic viscosity of $\nu = 10^{-5}$ in code units, following the "two first derivatives" formulation of the Navier–Stokes terms outlined in Section 3.2.4 of G. Lodato & D. J. Price (2010). This, is in addition to the usual shock capturing terms, which are implemented with the L. Cullen & W. Dehnen (2010), switch with $\alpha_{\rm av} \in [0, 1]$ and $\beta_{\rm av} = 2$ as outlined in D. J. Price et al. (2018).

2.3. Results

In Figures 1–4, we present two-dimensional contour plots in a $\phi - r$ plane, showing the gas density, radial velocity, azimuthal velocity, and meridional velocity at three different heights after 500 planetary orbits of evolution: $Z/R = 0, 0.1$, and 0.3. These heights are chosen to cover a range of vertical layers that various molecular lines having different optical depths probe (M. Galloway-Sprietsma et al. 2025; see also review by A. Miotello et al. 2023 and references therein). For a more quantitative comparison, we present one-dimensional azimuthal distributions of the gas density, radial velocity, azimuthal velocity, and meridional velocity in the Appendix.

[29] https://github.com/danieljprice/phantom/releases/tag/v2022.0.1

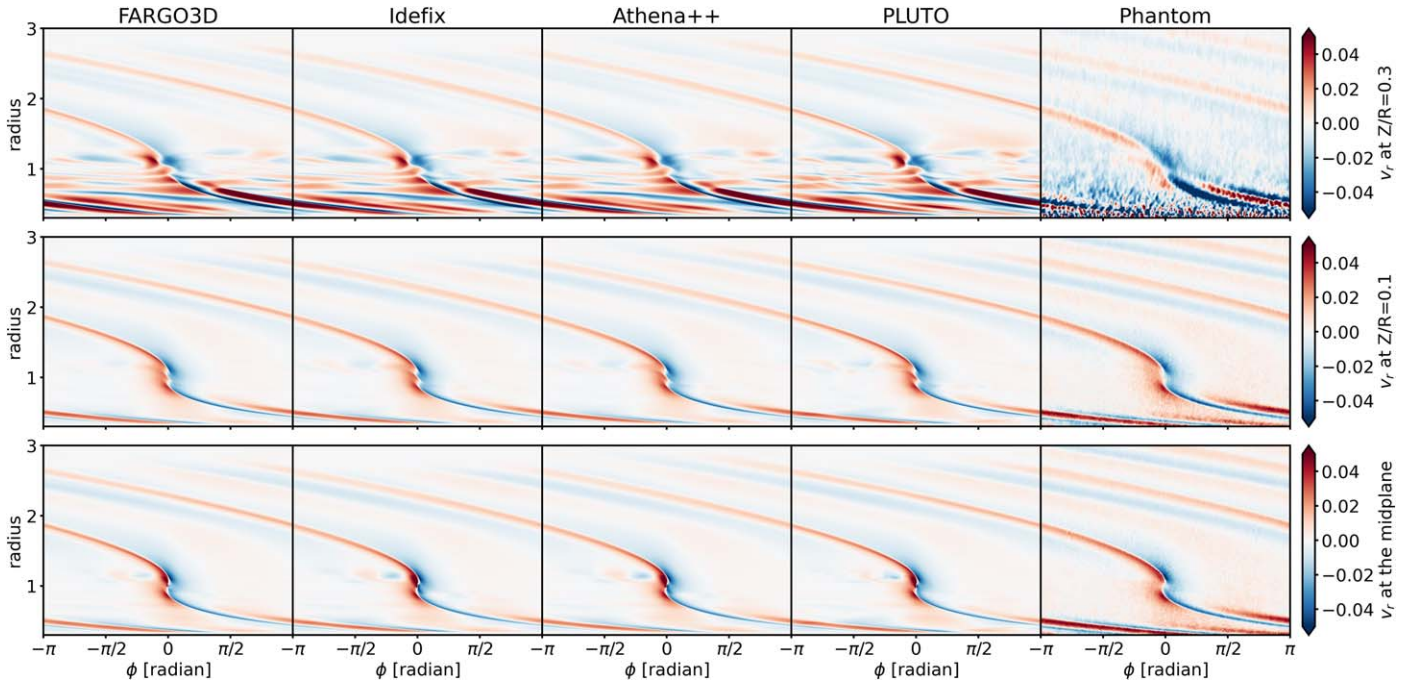

Figure 2. Same as Figure 1, but for the radial velocity v_r.

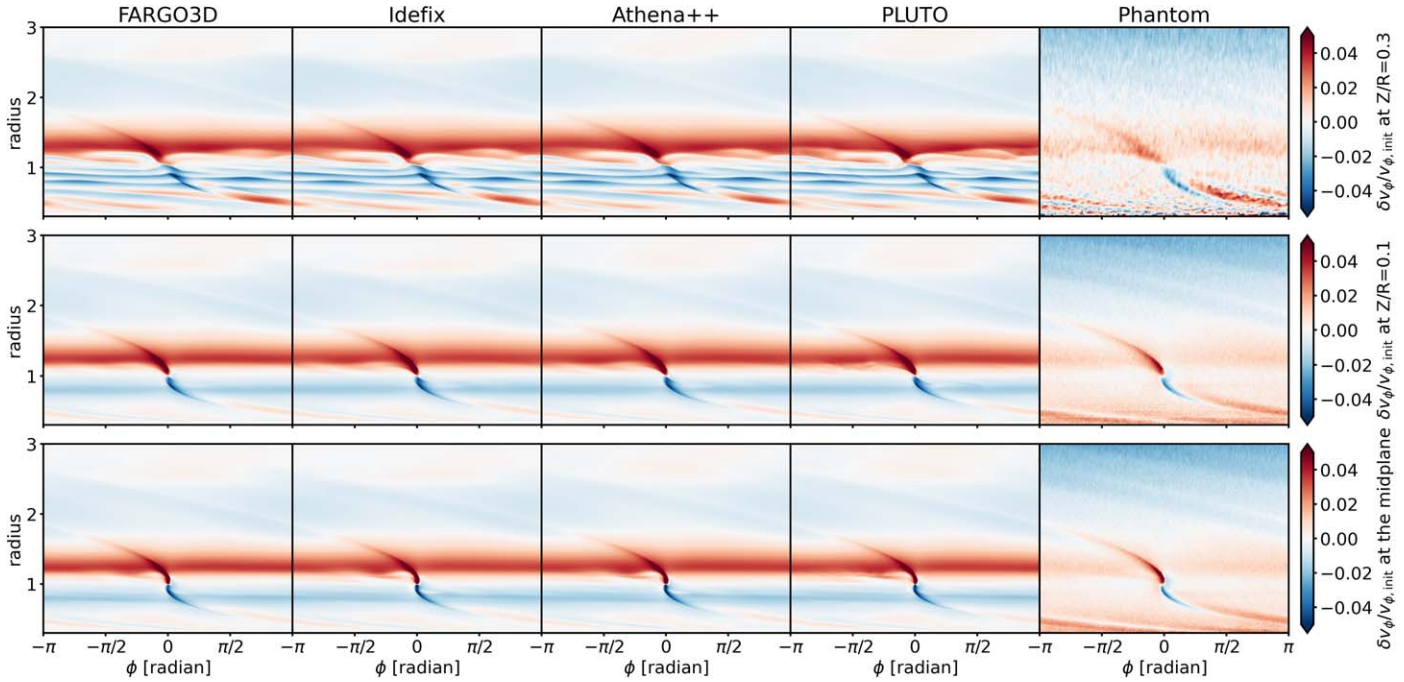

Figure 3. Same as Figure 1, but for the perturbed azimuthal velocity $\delta v_\phi \equiv v_\phi - v_{\phi,\mathrm{init}}$, normalized by the initial azimuthal velocity $v_{\phi,\mathrm{init}}$.

Looking first at the perturbed density presented in Figure 1, all the grid-based simulations show excellent agreement with each other although the level of density perturbation may differ by up to a few percent in the upper layers. Because particles can freely flow through the inner and outer boundaries, the `Phantom` simulation shows lower density near the radial boundaries. At the inner disk in particular, the low density results in a higher numerical viscosity. Together with strong shock dissipation in the inner disk, this leads to a rapid depletion, which in turn flattens the surface density profile and makes the planet-opened gap shallower. We caution that inferring the mass of gap-opening planet based on the gap shape from `Phantom` simulations could result in an overestimation. Nevertheless, we emphasize that the overall morphology of the spirals driven by the planet and the level of density perturbation associated with the spirals seen in the `Phantom` simulation agree well with those seen in grid-based simulations, presumably because they are not sensitive to the underlying surface density profile (G. I. Ogilvie & S. H. Lubow 2002; R. R. Rafikov 2002; J. Bae & Z. Zhu 2018).

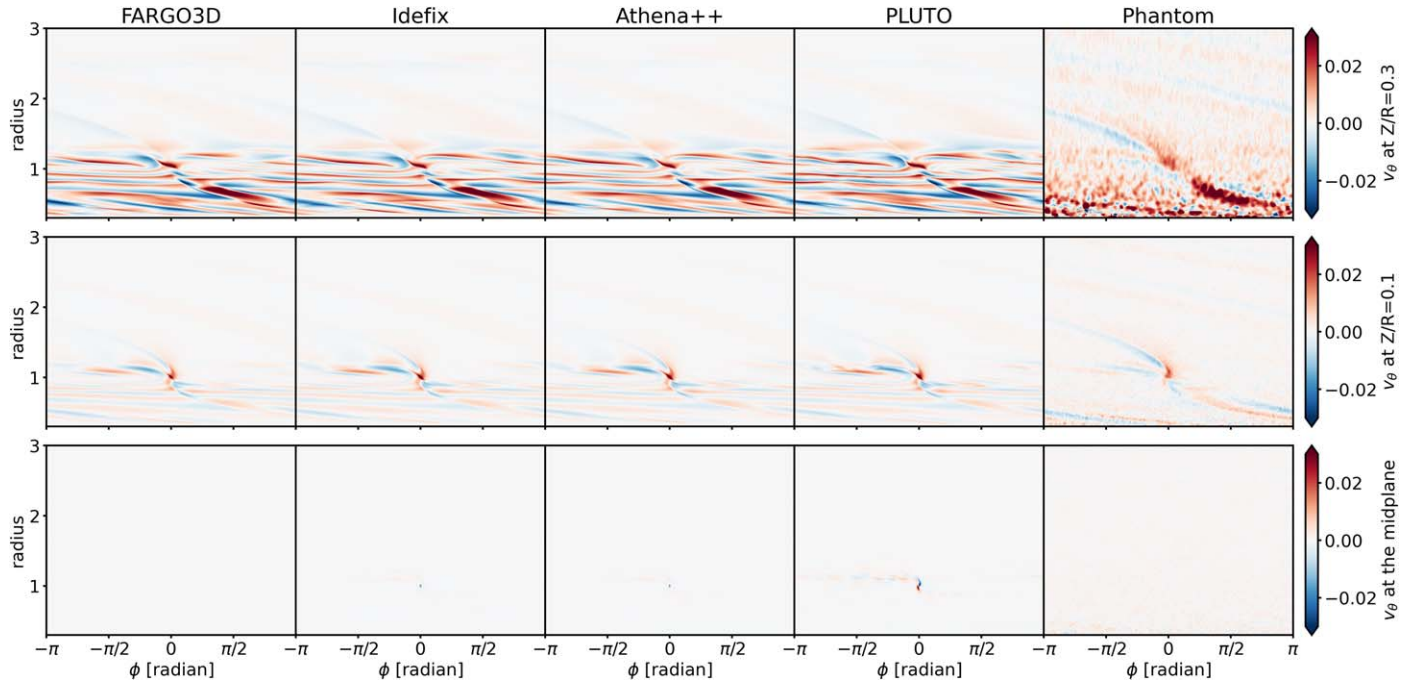

Figure 4. Same as Figure 1, but for the meridional velocity v_θ.

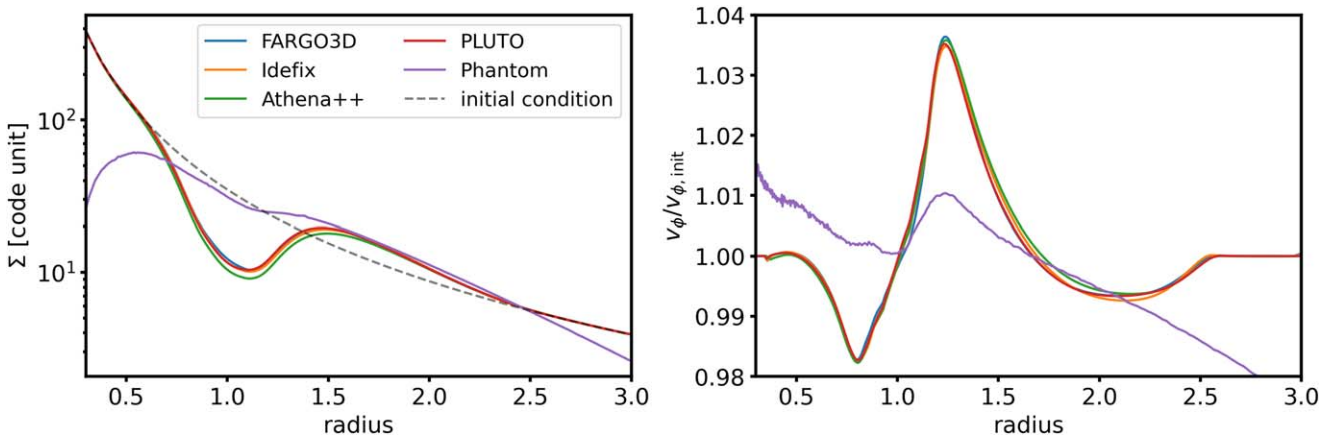

Figure 5. Radial profiles of the (left) surface density Σ and (right) azimuthal velocity at the midplane v_ϕ, normalized by the initial azimuthal velocity $v_{\phi,\mathrm{init}}$. While we present the azimuthal velocity at the midplane only, we confirm that the velocity at other heights shows a similar trend and good agreement between grid-based codes, with smaller velocity perturbations near the planet in the `Phantom` simulation due to the shallower gap.

Similarly to the density perturbation, velocity perturbations associated with the spirals show agreement among grid-based simulations (Figures 2–4). In the `Phantom` simulation, the perturbation in the azimuthal velocity across the gap is of the order of 1% of the Keplerian speed, much smaller than that in grid-based simulations (Figure 5), due to the shallower gap. However, the velocity perturbations along the spirals in the `Phantom` simulation are comparable to those in grid-based simulations. Because the strength of velocity kinks and Doppler flips is closely related to the level of velocity perturbations along the spirals, the consistency across all five hydrodynamics codes is important in the retrieval of the location of the planet, as we will show later in Section 4.

For a more quantitative comparison of the gap structure between the models, in Figure 5 we present azimuthally averaged radial profiles of the surface density and azimuthal velocity. In grid-based simulations, the surface density at the center of the gap opened by a Jupiter-mass planet is suppressed by $\simeq$70%. On the other hand, in the `Phantom` simulation, the surface density is decreased by only $\simeq$10%. The shallow gap results in an azimuthal velocity variation across the gap of $\sim$1%, much smaller than the $\sim$6% seen in grid-based codes.

3. Radiative Transfer Calculations

Radiative transfer calculations were carried out using `mcfost`[30] version 4.1.08 (C. Pinte et al. 2006; C. Pinte et al. 2009) and `RADMC-3D`[31] version 2.0 (C. P. Dullemond et al. 2012), using the outputs at 500 planetary orbits from the hydrodynamic simulations introduced in Section 2. As part of the exoALMA collaboration, the `mcfost` code was updated to natively read the output files from all hydrodynamic codes. We

[30] https://github.com/cpinte/mcfost/releases/tag/v4.1.08
[31] https://github.com/dullemond/radmc3d-2.0 (git commit ID: d80a15e).

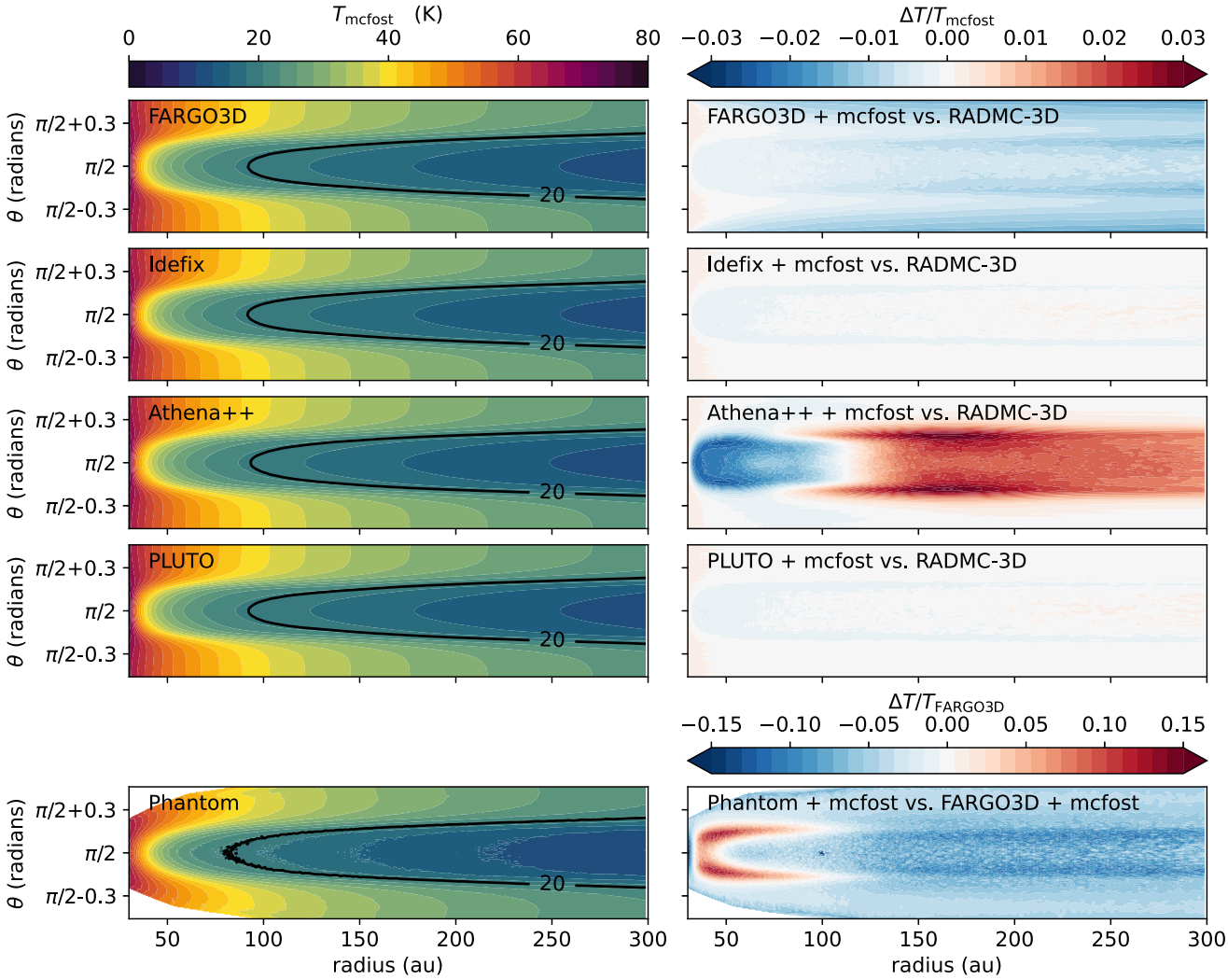

Figure 6. Azimuthally averaged temperature profiles in an $r-\theta$ plane from various combinations of hydrodynamic and radiative transfer codes (shown in the upper left corner of each panel). The black contours show where $T = 20$ K. The white areas in the upper left and lower left corners of the bottom panels is due to the lack of SPH particles there.

tested all the combinations between hydrodynamic and radiative transfer codes, except for the `Phantom` + `RADMC-3D` combination because at the time we wrote this Letter, there was no `RADMC-3D` module that allows one to read in `Phantom` outputs and map SPH particles onto a structured `RADMC-3D` grid. This results in a total of nine combinations.

3.1. Radiative Transfer Calculation Setup

We set the radiative transfer grid to be identical to that of grid-based hydrodynamic simulations described in Section 2.1.1. For `Phantom` outputs, we used a Voronoi tessellation where each `mcfost` cell corresponds to an SPH particle in order to avoid interpolating the density structure between the SPH and radiative transfer codes.

To convert physical quantities from dimensionless hydrodynamic simulations into physical units for radiative transfer calculations, we placed the planet at 100 au from the solar-mass central star. The total initial gas mass in the disk was set to $0.01\,M_{\odot}$. With this conversion, the initial gas surface density at the radial location of the planet is $0.52\,{\rm g\,cm^{-2}}$, which is broadly consistent with the gas surface density inferred for exoALMA disks (G. Rosotti et al. 2025). The star was placed at 140 pc from the observer.

To generate synthetic ^{12}CO $J = 3$–2 line cubes, we first determined the dust temperature by running Monte Carlo simulations. We placed a solar-mass star having a radius of $2\,R_{\odot}$ and a temperature of 4000 K at the center of the domain, which emits a total of 10^9 photons that interact with dust grains. Dust opacities were calculated assuming a power-law grain size distribution following $dn(a)/da \propto a^{-3.5}$, between $a_{\rm min} = 0.03$ μm and $a_{\rm max} = 1$ mm. The total dust mass was assumed to be 1% of the gas mass in each grid cell. Grain composition was assumed to be astrosilicates (J. C. Weingartner & B. T. Draine 2001). We computed the dust optical properties using the Mie theory, considering isotropic scattering only. The same opacities were used for both `mcfost` and `RADMC-3D` Monte Carlo simulations.

We assumed that the gas and dust are in local thermodynamic equilibrium, sharing the same temperature. We adopted a ^{12}CO abundance of 10^{-4} relative to the total gas (by number) when the temperature is higher than 20 K. Below 20 K, we assumed that all CO molecules are frozen onto grains and no gas phase CO is present. We made an assumption that

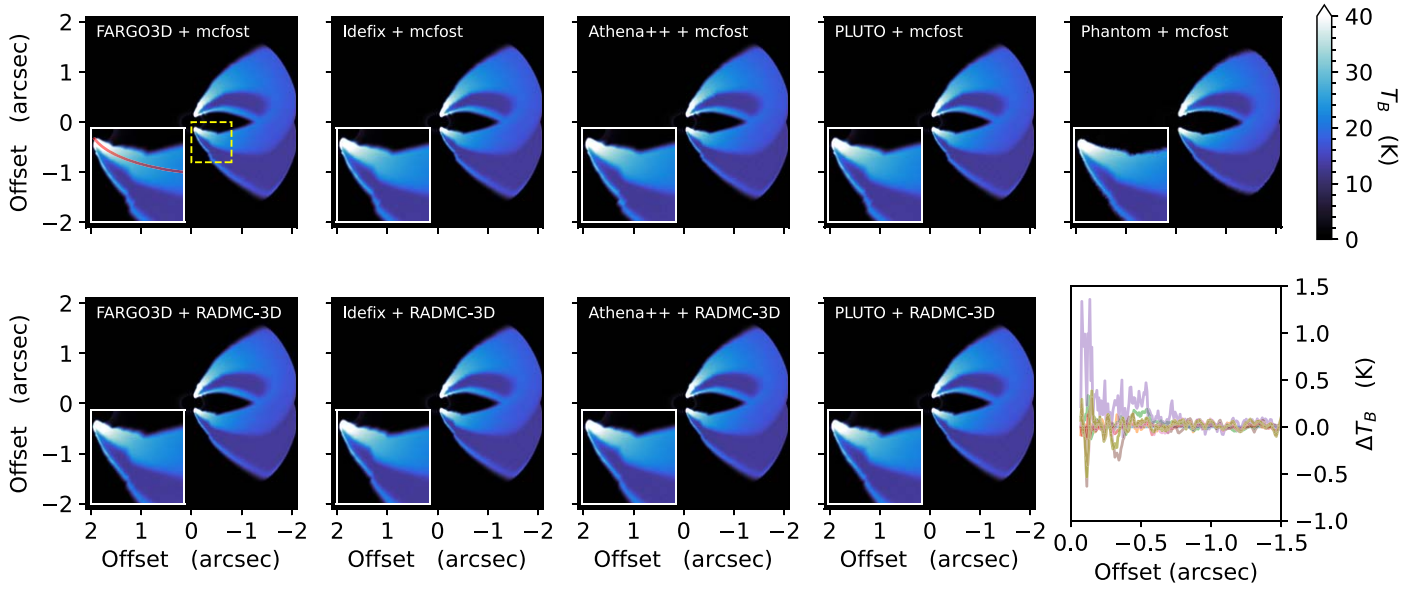

Figure 7. ^{12}CO channel maps at $v_{\rm los} = 1.1$ km s^{-1}, using various combinations of hydrodynamic and radiative transfer codes (code names shown in the upper left corner of each panel). The planet, embedded and thus invisible in the channel maps, is located 45° west of south. In all models, velocity kinks (indicated with a yellow dashed square in the upper left panel) are apparent in the vicinity of the planet. The inset in the lower left quadrant of each panel shows a zoomed-in view of the velocity kink. In the inset of the top left panel, we present the isovelocity contour with a red curve. The bottom right panel shows the brightness temperature along the isovelocity contour shown in the top left panel, compared to that of the `FARGO3D + mcfost` model. Note that the brightness temperature of all models agree well with each other.

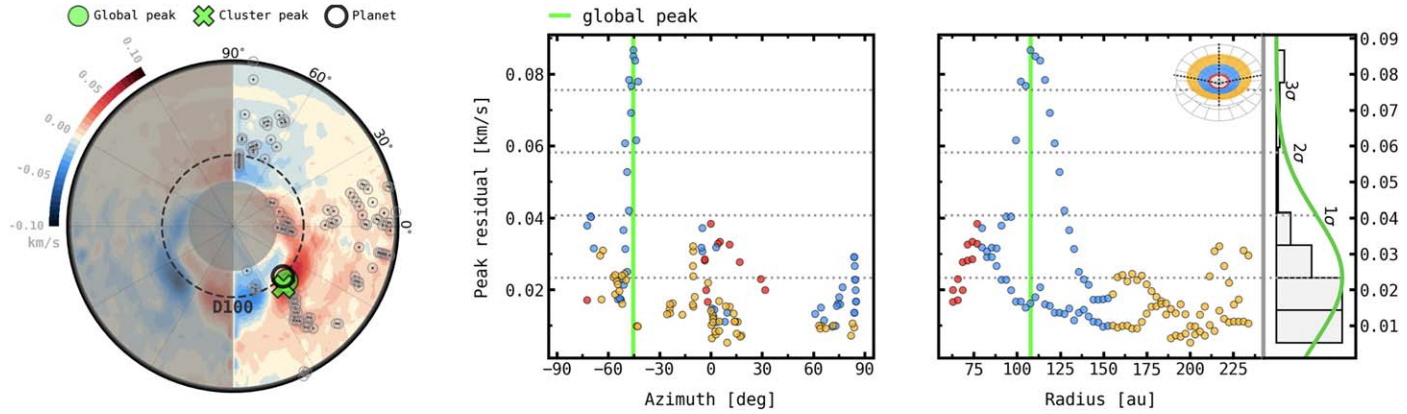

Figure 8. (Left panel) Folded velocity residual maps (see A. F. Izquierdo et al. 2023, 2025) computed for the ^{12}CO synthetic cube created with `FARGO3D` and `mcfost`, as an example. The green circle and cross indicate the location of peak and clustered residuals, whereas the black circle shows the correct planet location (100 au and −45°). (Middle panel) Peak residual velocity as a function of azimuthal angle. (Right panel) Peak residual velocity as a function of radius.

the local line width is set by thermal broadening only and ignored any nonthermal broadening.

The disk inclination was set to 45°, with a position angle of 90° (from north to east). The disk was placed at 140 pc and positioned such that the planet is located 45° west of south.

3.2. Results

3.2.1. Temperature

The left panels of Figure 6 present azimuthally averaged temperature distributions of the five `mcfost` models in an $r-\theta$ plane. The overall temperature structure exhibits a radially decreasing temperature profile, with a hotter atmosphere and a colder midplane, which is consistent with disk models where stellar irradiation is the dominating heating source (E. I. Chiang & P. Goldreich 1997; P. D'Alessio et al. 1998).

The temperature distributions show an excellent agreement within the four `mcfost` models using outputs from the grid-based hydrodynamics codes. When the azimuthally averaged two-dimensional temperature distributions are compared grid by grid, no two models have a temperature difference greater than 0.84 K (between `Idefix + mcfost` and `Athena++ + mcfost`), with a domain-averaged mean difference ranging from 0.013 K (between `FARGO3D + mcfost` and `PLUTO + mcfost`) to 0.18 K (between `Idefix + mcfost` and `Athena++ + mcfost`). In terms of fractional difference $\Delta T/T$, no two models have a difference greater than 2.7% (between `Idefix + mcfost` and `Athena++ + mcfost`) when compared grid by grid, with a domain-averaged mean difference ranging from 0.04% (between `FARGO3D + mcfost` and `Idefix + mcfost`) to 0.65% (between `Idefix + mcfost` and `Athena++ + mcfost`).

Similarly, excellent agreement was found among the `RADMC-3D` models. Based on grid-by-grid comparisons, we

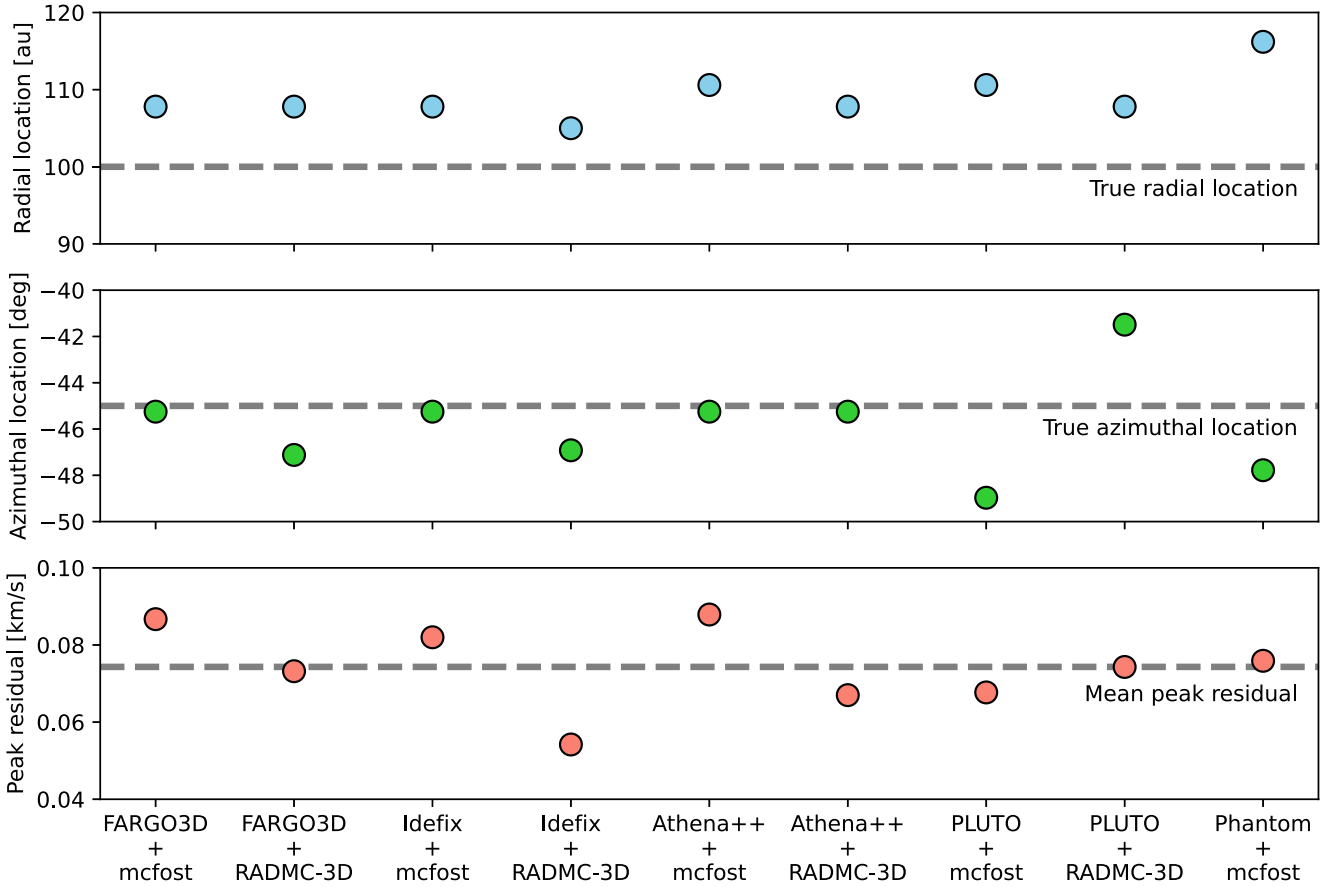

Figure 9. The (top) radial and (middle) azimuthal location of the planet inferred by DISCMINER (global peak in Figure 8) for synthetic ^{12}CO cubes generated with different combinations of hydrodynamic and radiative transfer codes. The bottom panel shows the peak residual velocity at the inferred planet location.

found no two models have a difference greater than 0.51 K (between FARGO3D + RADMC-3D and Athena++ + RADMC-3D). In terms of fractional difference, no two models have a difference greater than 1.8% (between FARGO3D + RADMC-3D and Athena++ + RADMC-3D).

When mcfost models are compared with RADMC-3D models, we found strong consistency between the models. Idefix and PLUTO models show excellent agreement in particular; when the temperatures are compared grid by grid, these models differ by only $\lesssim$0.08% on average. The Athena++ models show the largest differences, but even in this case, the fractional temperature difference is smaller than 3% everywhere in the domain. It is certainly worthwhile to further investigate why Athena++ models show larger differences, but as we will show in Section 3.2.2, the corresponding differences in ^{12}CO channel maps are smaller than the typical noise in the exoALMA data, and we defer such an investigation to a future study.

Lastly, we compared the Phantom + mcfost model to other mcfost models. As an example, we present the difference between the temperature profiles from the Phantom + mcfost model and FARGO3D + mcfost model in the bottom right panel of Figure 6. As shown, the Phantom model shows noticeable differences from other models, up to $\pm$15% in individual grid cells, with a domain-averaged mean difference of about 5%. Given the differences in the density structure we discussed in Section 2.3, this difference is not too surprising. Yet, this temperature difference results in only small differences in ^{12}CO channel maps and may not be noticeable in exoALMA-quality data, as we will show now.

3.2.2. Channel Maps

Figure 7 shows synthetic ^{12}CO emission at a representative velocity channel. Overall, the brightness temperature at the surface shows visually negligible differences among the models. In addition, all synthetic cubes show clear and consistent velocity kinks in the vicinity of the planet, which is crucial for retrieving planet mass and location. In the bottom right panel of Figure 7, we present the brightness temperature of each model relative to the reference model (FARGO3D + mcfost), along the isovelocity contour shown in the top left panel. As can be seen from the figure, all models agree with each other within $\pm$1.5 K, with the largest difference seen from the Phantom + mcfost model (lavender color). At the location of the planet (offset $\simeq -0\farcs5$), the difference among the models is $<$0.5 K. Given that the typical level of noise in the exoALMA molecular line images is about 1.5 K (R. Teague et al. 2025), we argue that the small, sub-Kelvin differences in brightness temperature among our models should not be a concern when it comes to modeling/finding embedded protoplanets.

4. Retrieval of Planet Location Using DISCMINER

We used DISCMINER[32] to retrieve the planet location in synthetic cubes. To do so, we convolved the raw synthetic cubes with a $0\farcs15$ Gaussian beam and added random noises with a standard deviation of 1.5 K in each 100 m s^{-1} channel; these are the beam size and level of noise of fiducial exoALMA

[32] https://github.com/andizq/discminer

molecular line images (R. Teague et al. 2025). For the detailed workflow of the retrieval, we refer the reader to A. F. Izquierdo et al. (2021, 2023).

In Figure 8, we present a folded velocity residual map for the ^{12}CO synthetic cube generated with FARGO3D and mcfost, along with peak residual velocity profile as a function of azimuthal angle and radius. DISCMINER found a peak in the folded velocity residual map with a 3.64σ significance and inferred the planet to be at 107.8 au in radius and $-45\overset{\circ}{.}25$ in azimuth, which are in a good agreement with the true planet location: 100 au and $-45°$.

To compare the inferred location of the planet and the associated peak velocity residual, we plot these quantities in Figure 9. Overall, the radial and azimuthal locations of the planet are consistent across the models and agree well with the true planet location. However, we found that the inferred radial locations are systematically biased toward slightly large radial distances with a mean distance of 109.0 au, a minimum distance of 105.0 au (Idefix + RADMC-3D), and a maximum distance of 116.2 au (Phantom + mcfost). This bias in radial location was previously noted in A. F. Izquierdo et al. (2021), too, and we speculate that this bias is because the peak residual is generally more sensitive to the outer spiral arm. Note, however, that the mean retrieved radial location is within one beam (0.″15, or 21 au at 140 pc) from the true location. In the case of the inferred azimuthal location, they are clustered around the true location with a mean azimuthal angle of $-45\overset{\circ}{.}92$, a minimum azimuthal angle of $-48\overset{\circ}{.}97$ (PLUTO + mcfost), and a maximum azimuthal angle of $-41\overset{\circ}{.}49$ (PLUTO + RADMC-3D). Lastly, we found that the peak residual velocity is broadly consistent within about 20% variation among the models, with a mean of 0.074 km s^{-1}, a minimum of 0.054 km s^{-1} (Idefix + RADMC-3D), and a maximum of 0.088 km s^{-1} (Athena++ + mcfost).

In summary, synthetic observations produced by any combination of the hydrodynamics and radiative transfer codes tested in this work exhibit broadly consistent localized perturbations near the true planet location.

5. Conclusion

To demonstrate the consistency of the codes used for forward-modeling protoplanetary disks from the community, we conducted a systematic comparison of various hydrodynamics and radiative transfer codes. To do so, we first carried out three-dimensional planet–disk interaction simulations using four grid-based hydrodynamics codes (FARGO3D, Idefix, Athena++, PLUTO) and an SPH code (Phantom). Overall, we found excellent agreement between grid-based codes, in terms of the density and velocity structure. However, due to the different boundary conditions in the Phantom simulation, we found that the planet-opened gap is shallower than those in grid-based simulations, which results in smaller azimuthal velocity deviations from the Keplerian rotation. Despite the difference in the gap depth, the overall morphology of the planet-driven spirals and the level of density/velocity perturbations associated with the spirals in the Phantom simulation are in a good agreement with those in other hydrodynamics codes.

We used two radiative transfer codes (mcfost and RADMC-3D) to calculate the disk temperature and generate synthetic ^{12}CO cubes. The disk temperatures showed good agreement within mcfost cubes and RADMC-3D cubes separately, as well as between mcfost and RADMC-3D models based on the same hydrodynamic simulation. Due to the different density structure, the disk temperature in the Phantom + mcfost model is different from other models, up to ±15% in individual grid cells, with a domain-averaged mean difference of about 5%. However, the corresponding difference in ^{12}CO emission is $\leqslant$1.5 K, within the typical noise in the exoALMA data.

Using DISCMINER, we retrieved the location of the planet from the synthetic cubes. Despite some differences in the hydrodynamics and/or radiative transfer calculation results, the retrieved planet locations are consistent across all cubes and agree well with the true planet location. This is because the density and velocity perturbations along the planet-driven spirals, which determines the location and strength of the velocity kink in channel maps, are consistent across all the codes we tested.

In summary, our findings suggest that any combination of the hydrodynamics and radiative transfer codes we tested in this Letter could be used to model and interpret planet-driven kinematic perturbations. Admittedly, we only considered one base hydrodynamic model. Future studies are needed to confirm that the consistency across all codes holds when changes are made to the model, such as planet mass, orbital migration, vertical temperature stratification, finite gas cooling time, disk viscosity, and the presence/strength of disk's magnetic fields.

Acknowledgments

This Letter makes use of the following ALMA data: ADS/JAO.ALMA#2021.1.01123.L. ALMA is a partnership of ESO (representing its member states), NSF (USA) and NINS (Japan), together with NRC (Canada), MOST and ASIAA (Taiwan), and KASI (Republic of Korea), in cooperation with the Republic of Chile. The Joint ALMA Observatory is operated by ESO, AUI/NRAO and NAOJ. The National Radio Astronomy Observatory is a facility of the National Science Foundation operated under cooperative agreement by Associated Universities, Inc. We thank the North American ALMA Science Center (NAASC) for their generous support including providing computing facilities and financial support for student attendance at workshops and publications. Part of the calculations were performed on the OzSTAR national facility at Swinburne University of Technology. The OzSTAR program receives funding in part from the Astronomy National Collaborative Research Infrastructure Strategy (NCRIS) allocation provided by the Australian Government, and from the Victorian Higher Education State Investment Fund (VHESIF) provided by the Victorian Government. J.B. acknowledges support from NASA XRP grant No. 80NSSC23K1312. M.B., D.F., and J.S. have received funding from the European Research Council (ERC) under the European Union's Horizon 2020 research and innovation program (PROTOPLANETS, grant agreement No. 101002188). Computations by J.S. have been performed on the "Mesocentre SIGAMM" machine, hosted by Observatoire de la Cote d'Azur. P.C. acknowledges support by the Italian Ministero dell'Istruzione, Università e Ricerca through the grant Progetti Premiali 2012 - iALMA (CUP C52I13000140001) and by the ANID BASAL project FB210003. N.C. has received funding from the European Research Council (ERC) under the European Union Horizon Europe research and innovation program (grant agreement No. 101042275, project Stellar-MADE). S.F. is funded by the European Union (ERC, UNVEIL, 101076613), and acknowledges financial contribution from PRIN-MUR 2022YP5ACE. MF is supported by a grant-in-Aid from the Japan Society for

the Promotion of Science (KAKENHI: No. JP22H01274). C.H. acknowledges support from NSF AAG grant No. 2407679. I.H. is supported by an Australian Government Research Training Program (RTP) Scholarship. Support for AFI was provided by NASA through the NASA Hubble Fellowship grant No. HST-HF2-51532.001-A awarded by the Space Telescope Science Institute, which is operated by the Association of Universities for Research in Astronomy, Inc., for NASA, under contract NAS5-26555. G.L. has received funding from the European Union's Horizon 2020 research and innovation program under the Marie Sklodowska-Curie grant agreement No. 823823 (DUSTBUSTERS). C.L. has received funding from the European Union's Horizon 2020 research and innovation program under the Marie Sklodowska-Curie grant agreement No. 823823 (DUSTBUSTERS) and by the UK Science and Technology research Council (STFC) via the consolidated grant ST/W000997/1. C.P. acknowledges Australian Research Council funding via FT170100040, DP18010423, DP220103767, and DP240103290. D.P. acknowledges Australian Research Council funding via DP18010423, DP220103767, and DP240103290. G.R. acknowledges funding from the Fondazione Cariplo, grant no. 2022-1217, and the European Research Council (ERC) under the European Union's Horizon Europe Research & Innovation Programme under grant agreement no. 101039651 (DiscEvol). G.W.F. acknowledges support from the European Research Council (ERC) under the European Union Horizon 2020 research and innovation program (grant agreement no. 815559 (MHDiscs)). G.W.F. was granted access to the HPC resources of IDRIS under the allocation A0120402231 made by GENCI. T.C.Y. acknowledges support by grant-in-Aid for JSPS Fellows JP23KJ1008. Views and opinions expressed by ERC-funded scientists are however those of the author(s) only and do not necessarily reflect those of the European Union or the European Research Council. Neither the European Union nor the granting authority can be held responsible for them.

Software: `FARGO3D` (P. Benítez-Llambay & F. S. Masset 2016), `Idefix` (G. R. J. Lesur et al. 2023), `Athena++` (J. M. Stone et al. 2020), `PLUTO` (A. Mignone et al. 2007), `Phantom` (D. J. Price et al. 2018), `mcfost` (C. Pinte et al. 2022), `RADMC-3D` (C. P. Dullemond et al. 2012), `DISCMINER` (A. F. Izquierdo et al. 2021).

Appendix
Azimuthal Density and Velocity Profiles

In Figures 10–13, we present azimuthal distributions of the density, radial velocity, azimuthal velocity, and meridional velocity at $R = 0.7$ and $R = 1.3$. In each figure, we present the azimuthal distributions at three different heights, $Z/R = 0, 0.1$, and 0.3.

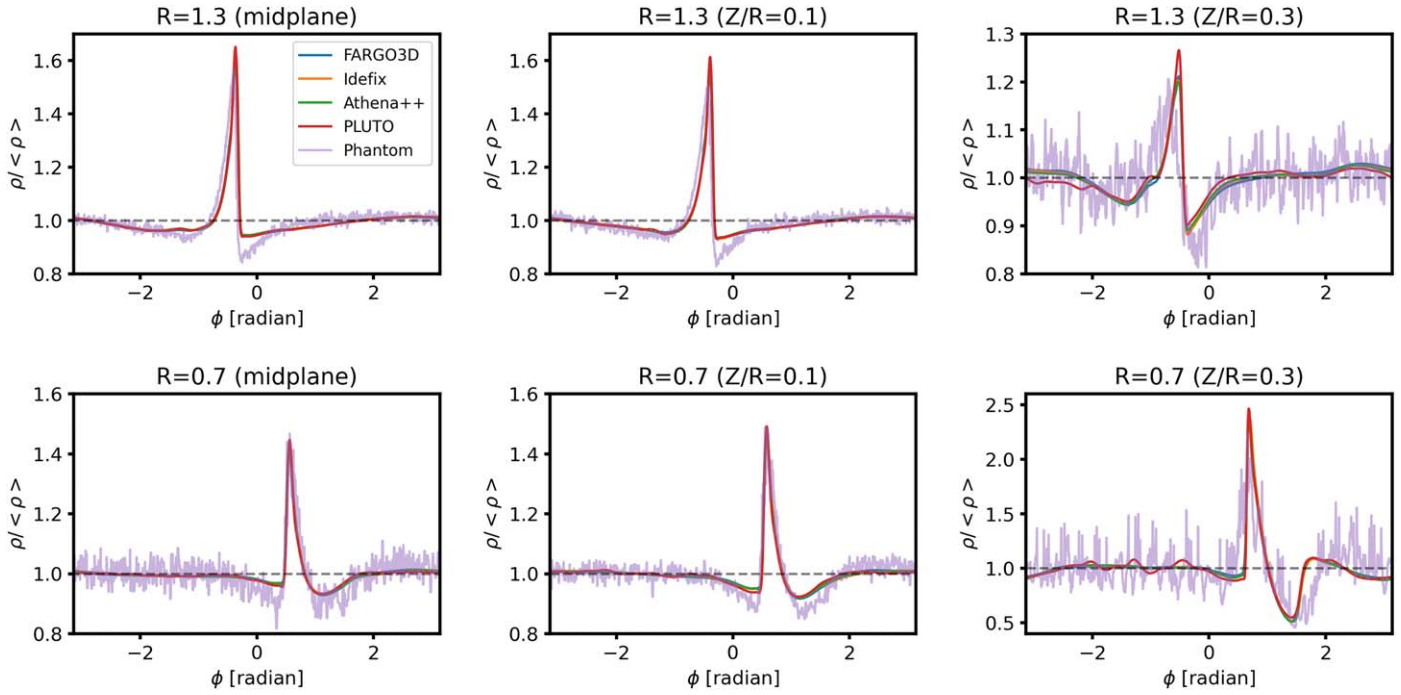

Figure 10. Azimuthal distribution of the density at (top panels) $R = 1.3$ and (bottom panels) $R = 0.7$. From left to right, each panel shows the density at the midplane, at $Z/R = 0.1$, and at $Z/R = 0.3$, respectively. The scatter seen in the `Phantom` simulation is due to the finite number of particles used in the simulation and is expected.

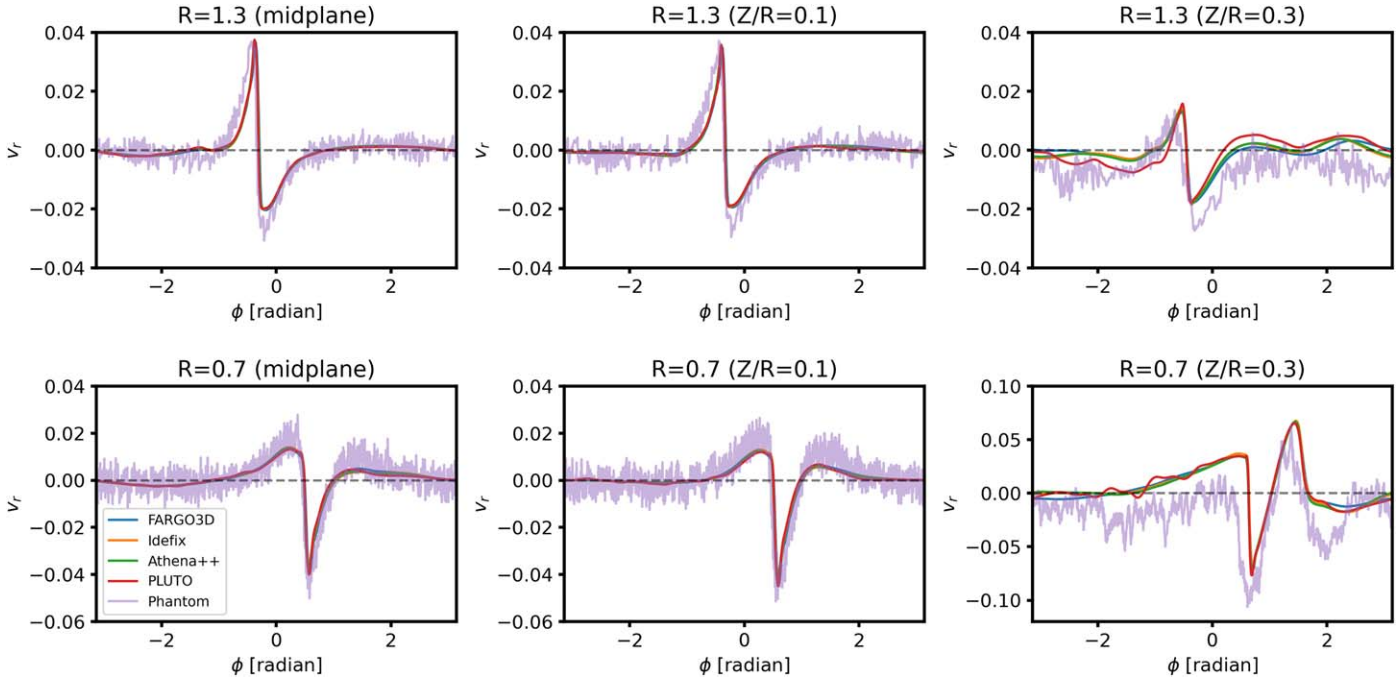

Figure 11. Same as Figure 10, but for the radial velocity v_r.

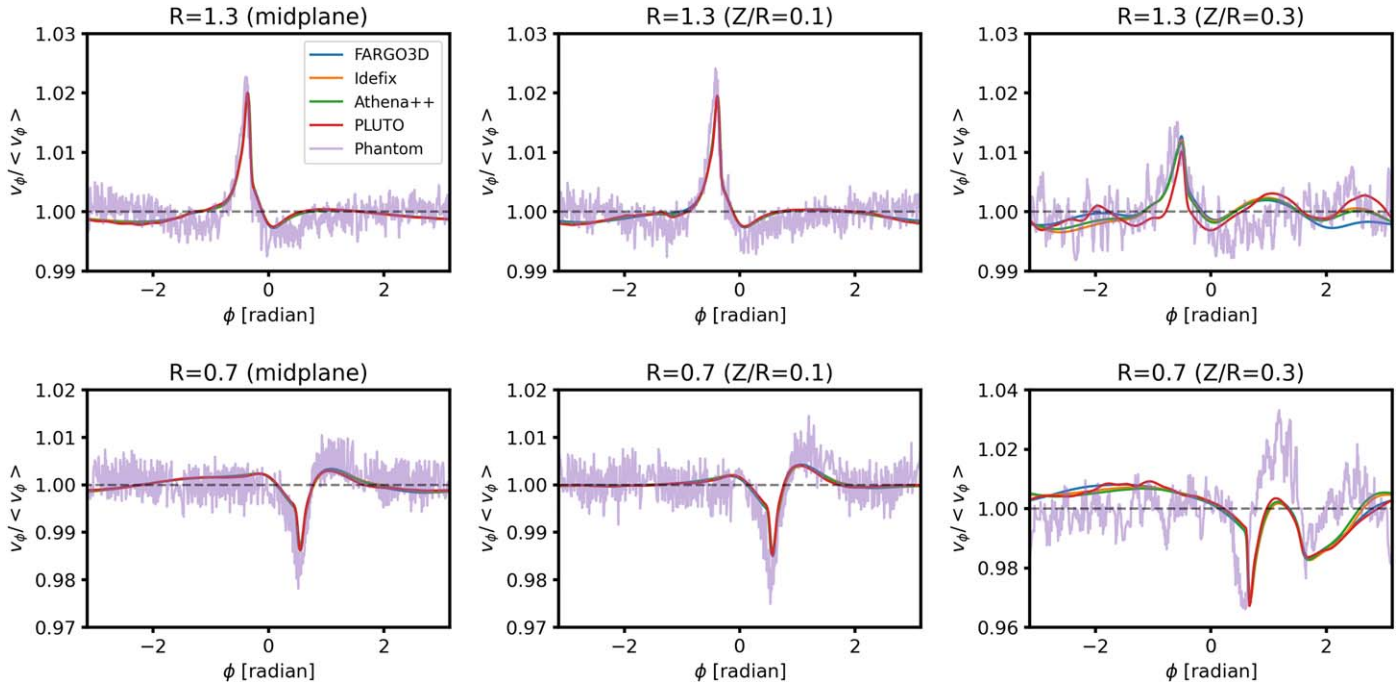

Figure 12. Same as Figure 10, but for the azimuthal velocity $v_\phi/\langle v_\phi \rangle$.

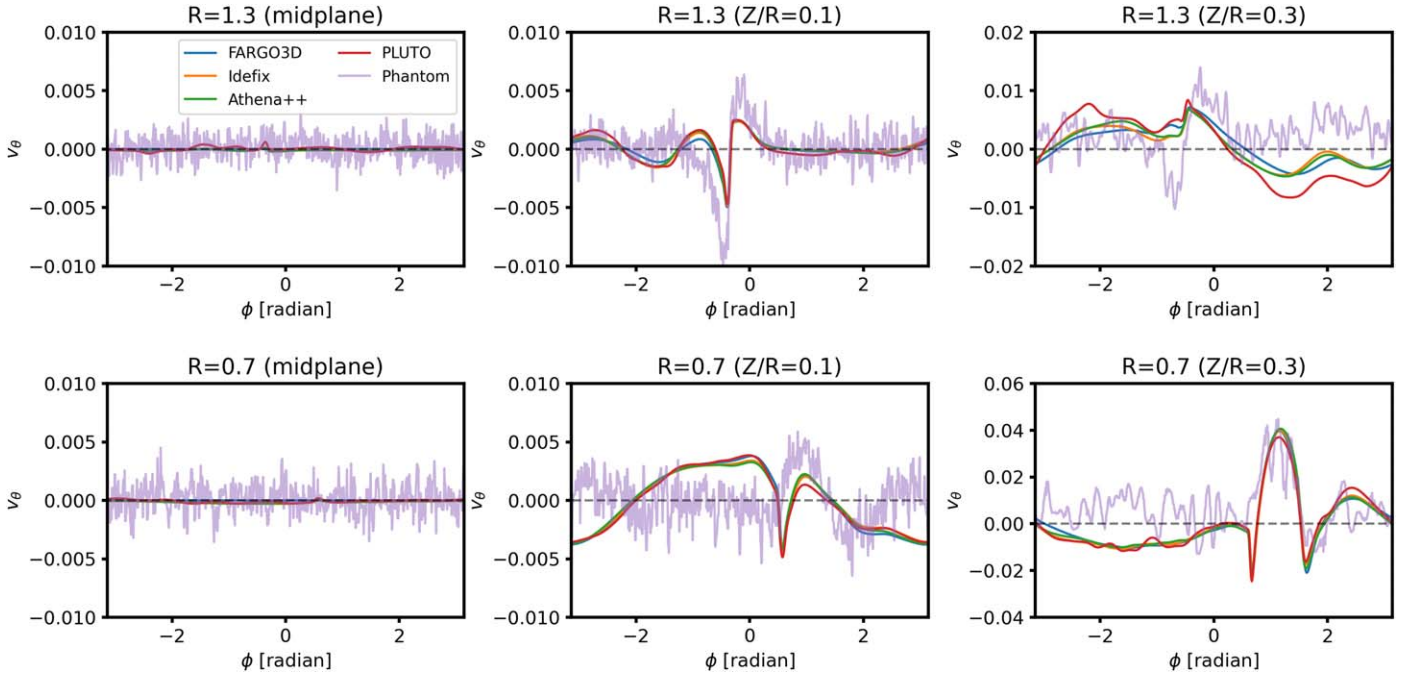

Figure 13. Same as Figure 10, but for the meridional velocity v_θ.

ORCID iDs

Jaehan Bae https://orcid.org/0000-0001-7258-770X
Mario Flock https://orcid.org/0000-0002-9298-3029
Andrés Izquierdo https://orcid.org/0000-0001-8446-3026
Kazuhiro Kanagawa https://orcid.org/0000-0001-7235-2417
Tomohiro Ono https://orcid.org/0000-0001-8524-6939
Christophe Pinte https://orcid.org/0000-0001-5907-5179
Daniel J. Price https://orcid.org/0000-0002-4716-4235
Giovanni P. Rosotti https://orcid.org/0000-0003-4853-5736
Gaylor Wafflard-Fernandez https://orcid.org/0000-0002-3468-9577
Geoffroy Lesur https://orcid.org/0000-0002-8896-9435
Frédéric Masset https://orcid.org/0000-0002-9626-2210
Sean M. Andrews https://orcid.org/0000-0003-2253-2270
Marcelo Barraza-Alfaro https://orcid.org/0000-0001-6378-7873
Myriam Benisty https://orcid.org/0000-0002-7695-7605
Gianni Cataldi https://orcid.org/0000-0002-2700-9676
Nicolás Cuello https://orcid.org/0000-0003-3713-8073
Pietro Curone https://orcid.org/0000-0003-2045-2154
Ian Czekala https://orcid.org/0000-0002-1483-8811
Stefano Facchini https://orcid.org/0000-0003-4689-2684
Daniele Fasano https://orcid.org/0000-0003-4679-4072
Maria Galloway-Sprietsma https://orcid.org/0000-0002-5503-5476
Cassandra Hall https://orcid.org/0000-0002-8138-0425
Iain Hammond https://orcid.org/0000-0003-1502-4315
Jane Huang https://orcid.org/0000-0001-6947-6072
Giuseppe Lodato https://orcid.org/0000-0002-2357-7692
Cristiano Longarini https://orcid.org/0000-0003-4663-0318
Jochen Stadler https://orcid.org/0000-0002-0491-143X
Richard Teague https://orcid.org/0000-0003-1534-5186
David J. Wilner https://orcid.org/0000-0003-1526-7587
Andrew J. Winter https://orcid.org/0000-0002-7501-9801
Lisa Wölfer https://orcid.org/0000-0002-7212-2416
Tomohiro C. Yoshida https://orcid.org/0000-0001-8002-8473

References

Andrews, S. M. 2020, ARA&A, 58, 483
Bae, J., Isella, A., Zhu, Z., et al. 2023, in ASP Conf. Ser. 534, Protostars and Planets VII, ed. S. Inutsuka et al. (San Francisco, CA: ASP), 423
Bae, J., Nelson, R. P., & Hartmann, L. 2016, ApJ, 833, 126
Bae, J., Teague, R., & Zhu, Z. 2021, ApJ, 912, 56
Bae, J., & Zhu, Z. 2018, ApJ, 859, 118
Bae, J., Zhu, Z., Baruteau, C., et al. 2019, ApJL, 884, L41
Bate, M. R., Bonnell, I. A., & Price, N. M. 1995, MNRAS, 277, 362
Benítez-Llambay, P., & Masset, F. S. 2016, ApJS, 223, 11
Chen, K., & Dong, R. 2024, ApJ, 976, 49
Chiang, E. I., & Goldreich, P. 1997, ApJ, 490, 368
Cullen, L., & Dehnen, W. 2010, MNRAS, 408, 669
D'Alessio, P., Cantö, J., Calvet, N., & Lizano, S. 1998, ApJ, 500, 411
de Val-Borro, M., Edgar, R. G., Artymowicz, P., et al. 2006, MNRAS, 370, 529
Dullemond, C. P., Juhasz, A., Pohl, A., et al., 2012 RADMC-3D: A Multi-purpose Radiative Transfer Tool, Astrophysics Source Code Library, ascl:1202.015
Galloway-Sprietsma, M., Bae, J., Izquierdo, A., et al. 2025, ApJL, 984, L10
Izquierdo, A. F., Stadler, J., Bae, J., et al. 2025, ApJL, 984, L8
Izquierdo, A. F., Testi, L., Facchini, S., et al. 2023, A&A, 674, A113
Izquierdo, A. F., Testi, L., Facchini, S., Rosotti, G. P., & van Dishoeck, E. F. 2021, A&A, 650, A179
Kanagawa, K. D., Tanaka, H., Muto, T., Tanigawa, T., & Takeuchi, T. 2015, MNRAS, 448, 994
Lesur, G. R. J., Baghdadi, S., Wafflard-Fernandez, G., et al. 2023, A&A, 677, A9
Lin, D. N. C., & Papaloizou, J. C. B. 1993, in Protostars and Planets III, ed. E. H. Levy & J. I. Lunine (Tucson, AZ: Univ. of Arizona Press), 749
Lodato, G., & Price, D. J. 2010, MNRAS, 405, 1212
Lyra, W., Richert, A. J. W., Boley, A., et al. 2016, ApJ, 817, 102
Masset, F. 2000, A&AS, 141, 165
Mignone, A., Bodo, G., Massaglia, S., et al. 2007, ApJS, 170, 228
Miotello, A., Kamp, I., Birnstiel, T., Cleeves, L. C., & Kataoka, A. 2023, in ASP Conf. Ser. 534, Protostars and Planets VII, ed. S. Inutsuka et al. (San Francisco, CA: ASP), 501
Muley, D., Melon Fuksman, J. D., & Klahr, H. 2024, A&A, 687, A213
Ogilvie, G. I., & Lubow, S. H. 2002, MNRAS, 330, 950
Pinte, C., Ilee, J. D., Huang, J., et al. 2025, ApJL, 984, L15
Pinte, C., Ménard, F., Duchêne, G., & Bastien, P. 2006, A&A, 459, 797
Pinte, C., Ménard, F., Duchêne, G., et al., 2022 MCFOST: Radiative Transfer Code, Astrophysics Source Code Library, ascl:2207.023
Pinte, C., Teague, R., Flaherty, K., et al. 2023, in ASP Conf. Ser. 534, Protostars and Planets VII, ed. S. Inutsuka et al. (San Francisco, CA: ASP), 645

Pinte, C., Price, D. J., Ménard, F., et al. 2018, ApJL, 860, L13
Pinte, C., van der Plas, G., Ménard, F., et al. 2019, NatAs, 3, 1109
Pinte, C., Harries, T. J., Min, M., et al. 2009, A&A, 498, 967
Price, D. J., Wurster, J., Tricco, T. S., et al. 2018, PASA, 35, e031
Rafikov, R. R. 2002, ApJ, 572, 566
Richert, A. J. W., Lyra, W., Boley, A., Mac Low, M.-M., & Turner, N. 2015, ApJ, 804, 95
Rosotti, G., Longarini, C., Paneque-Carreño, T., et al. 2025, ApJL, 984, L20
Shakura, N. I., & Sunyaev, R. A. 1973, A&A, 24, 337
Stone, J. M., Tomida, K., White, C. J., & Felker, K. G. 2020, ApJS, 249, 4
Teague, R., Benisty, M., Facchini, S., Fukagawa, M., Pinte, C., et al. 2025, ApJL, 984, L6
Weingartner, J. C., & Draine, B. T. 2001, ApJ, 548, 296
Yun, H.-G., Kim, W.-T., Bae, J., & Han, C. 2019, ApJ, 884, 142
Zhang, S., Zhu, Z., Huang, J., et al. 2018, ApJL, 869, L47